www.MaterialsViews.com

ADVANCED
FUNCTIONAL
MATERIALS
www.afm-journal.de

FULL PAPER

Engineering Gold Nanotubes with Controlled Length and Near-Infrared Absorption for Theranostic Applications

Sunjie Ye, Gemma Marston, James R. McLaughlan, Daniel O. Sigle, Nicola Ingram, Steven Freear, Jeremy J. Baumberg, Richard J. Bushby, Alexander F. Markham, Kevin Critchley, Patricia Louise Coletta, and Stephen D. Evans*

Important aspects in engineering gold nanoparticles for theranostic applications include the control of size, optical properties, cytotoxicity, biodistribution, and clearance. In this study, gold nanotubes with controlled length and tunable absorption in the near-infrared (NIR) region have been exploited for applications as photothermal conversion agents and in vivo photoacoustic imaging contrast agents. A length-controlled synthesis has been developed to fabricate gold nanotubes (NTs) with well-defined shape (i.e., inner void and open ends), high crystallinity, and tunable NIR surface plasmon resonance. A coating of poly(sodium 4-styrenesulfonate) (PSS) endows the nanotubes with colloidal stability and low cytotoxicity. The PSS-coated Au NTs have the following characteristics: i) cellular uptake by colorectal cancer cells and macrophage cells, ii) photothermal ablation of cancer cells using single wavelength pulse laser irradiation, iii) excellent in vivo photoacoustic signal generation capability and accumulation at the tumor site, iv) hepatobiliary clearance within 72 h postintravenous injection. These results demonstrate that these PSS-coated Au NTs have the ideal attributes to develop their potential as effective and safe in vivo imaging nanoprobes, photothermal conversion agents, and drug delivery vehicles. To the best of knowledge, this is the first in vitro and in vivo study of gold nanotubes.

1. Introduction

Photoacoustic imaging (PAI) is a non-invasive and nonionizing modality that combines the spectral selectivity of laser excitation with the high resolution of ultrasound imaging. In PAI, an absorbed laser pulse induces rapid thermal expansion at the target leading to the generation of acoustic waves that are detected by ultrasonic transducers to form images. By tuning the incident light into specific molecular absorption bands, PAI has been able to, for example, map the oxygenation state of hemoglobin or to map different chemical distributions in vivo.[1] For applications where no natural contrast is available, contrast agents, such as indocyanine green, have been demonstrated to be effective.[2]

Photothermal therapy, also known as photothermal ablation or optical hyperthermia, has been actively explored as a minimally invasive approach to cancer therapy. It utilizes photothermal conversion agents (PTCAs), which strongly absorb light and convert the absorbed light into heat, to generate rapid localized heating to preferentially ablate cancerous cells.[3]

Key criteria for the development of PAI contrast agents and PTCAs are, first, they should have strong absorbance in the near-infrared (NIR) tissue transparent region of the EM spectrum (650–900 nm) which is ideal for optical imaging and photothermal therapy,[4] and second, they should have low toxicity.

Gold nanostructures have been recently developed as versatile, multifaceted platforms for a broad range of biomedical applications, which include biosensing, photothermal therapy, targeted drug delivery, and bioimaging (e.g., optical coherence tomography, two-photon luminescence, and photoacoustic techniques).[5] The development of Au nanostructures as contrast agents is based on the ability to tune their optical properties via control over the localized surface plasmon modes.[4] The photoacoustic signal-to-noise ratio can be significantly improved by carefully choosing the excitation laser wavelength within NIR region to minimize the light attenuation.[6] Hence, considerable efforts have been made to develop Au nanostructures active in the NIR window, such as Au nanorods, Au nanoshells, hollow

Dr. S. Ye, Prof. R. J. Bushby, Dr. K. Critchley, Prof. S. D. Evans
School of Physics and Astronomy
University of Leeds
Leeds LS2 9JT, UK
E-mail: S.D.Evans@leeds.ac.uk
Dr. S. Ye, Dr. G. Marston, Dr. N. Ingram, Prof. A. F. Markham, Dr. P. L. Coletta
Leeds Institute for Biomedical and Clinical Sciences
University of Leeds
Leeds LS9 7TF, UK
Dr. J. R. McLaughlan, Dr. S. Freear
School of Electronic and Electrical Engineering
University of Leeds
Leeds LS2 9JT, UK
D. O. Sigle, Prof. J. J. Baumberg
NanoPhotonics Centre
Cavendish Laboratory
University of Cambridge
Cambridge CB3 0HE, UK

FULL PAPER

Au nanospheres, and Au nanocages. These NIR-absorbing gold nanostructures have been exploited as theranostic nanosystems that integrate targeting, imaging, and therapy (chemotherapy via drug delivery and photothermal therapy) into one platform.[7–10] As a novel nanostructure with promise for theranostic applications, Au nanotubes (NTs) offer potential advantages over their solid counterparts. First, as open-ended tubes they have large inner voids that can be filled with suitable drugs from small molecules through to proteins. Second, they have inner and outer surfaces, which might provide routes for differential surface functionalization enabling selective attachment of moieties to the inside (such as drugs and imaging agents) and outside (targeting moieties, antifouling agents). Third, they have open ends that make the inner surface accessible and allow subsequent incorporation of species within the tubes and can be used as a gate to control drug release.[11,12] In addition, for photoacoustic imaging and photothermal therapy, the hollow core can lower the heat capacity to allow better pulse heating.[13] Compared to their spherical counterparts, the elongated nanostructures have longer blood circulation times[14] and show multivalence effect, that is, multiple binding sites of a functionalized NT to one cell, leading to improved cell adhesion and more effective targeting.[15]

However, to date, little work has been undertaken on the biomedical application of Au NTs because of the limited control over their length and uniformity coupled with the lack of NIR optical absorption. Therefore, it is essential to develop synthesis routes that allow good control over the NT length and fine-tuning their optical behavior in the NIR region.

A major concern related to biomedical application of Au nanoparticles is their in vivo metabolism and toxicity. While little acute and subacute toxicity has been observed from in vivo administration of therapeutic Au nanoparticles,[16] chronic toxicological investigations have shown that after a single intravenous injection in rat, 40 nm gold nanoparticles accumulated in liver throughout the entire timeframe of the study (two months) and caused changes of gene expression in the liver and spleen.[17] An irreversible change in the proteomic profile was observed in the liver of mice receiving PEG-coated hollow Au nanospheres.[18] With respect to maintenance of reticuloendothelial (RES) organ function, protection from chronic inflammation, mutagenicity, and effects on reproductive health, it is necessary to facilitate hepatobiliary clearance of Au nanoparticles used for imaging or therapy.[16]

Here, we present the synthesis of Au NTs of controlled length, over the range of 300– 700 nm, via the room-temperature galvanic displacement of silver nanorods (Ag NRs). The resultant Au NTs show strong surface plasmon resonance (SPR)-based absorption in the NIR region, which can be tuned by varying the NT length or the composition of the nanotube. Poly(sodium 4-styrenesulfonate) (PSS) coating of the gold nanotubes imparts colloid stability and low cytotoxicity. In vitro cell studies demonstrate that, PSS–Au NTs can be internalized by cancer cells (SW480 cells) and macrophages (RAW 264.7). NIR laser irradiation caused photothermal ablation of the cancer cells that had internalized PSS–Au NTs. The PSS–Au NTs also displayed strong in vivo photoacoustic signals and accumulation at the SW620 tumor site, enabling them to be used as effective PAI contrast agents. Furthermore, investigation of the

in vivo biodistribution of the PSS–Au NTs showed hepatobiliary clearance within 72 h, demonstrating that PSS–Au NTs are suitable for clinical translation.

To our knowledge, the present work represents the first in vitro and in vivo study of gold nanotubes and demonstrates their effectiveness as novel agents for photoacoustic imaging and photothermal therapy with a potential of drug delivery, to achieve image-guided combined chemo-photothermal therapy.

2. Results and Discussion

2.1. Synthesis and Length Control of Gold Nanotubes

The formation of hollow Au nanostructures via the galvanic replacement of metallic template by Au (III) ions has received significant interest due to its simplicity and because of the homogeneous and highly crystalline nature of the structures formed.[19,20] In the present work, Au NTs were formed via the galvanic displacement of Ag NRs of controlled length. The Ag NRs were grown from Ag seeds using PSS as a structure-directing agent.[21] This involved two steps: 1) generation of Ag seeds ($D = 4$ nm) by chemical reduction of $AgNO_3$ by $NaBH_4$ in the presence of trisodium citrate to stabilize the nanoparticles[22] and 2) formation of Ag NRs upon addition of the Ag seeds to a growth solution containing $AgNO_3$, ascorbic acid, and PSS. The resultant Ag NRs had pentagonal cross-section, five flat side surfaces bounded by {100} facets and ten {111} end facets. It was found that, by adjusting the seed amount and growth temperature we could obtain improved control over the nanorod length. Previous reports of this approach produced significantly longer NR, typically, of the order 1 µm.[21] In contrast, the Ag NRs produced here could be controlled with lengths down to 300 nm, and by controlling the growth temperature we have been able to greatly improve the reproducibility for synthesizing Ag NRs of a desired length.

Figure 1 shows scanning electron microscopy (SEM) images of Ag NRs synthesized at 25 °C by adding different volumes of seed dispersion into the growth solution. The resultant Ag NRs had a uniform diameter of 50 nm and the lengths that varied inversely with seed amount. The NRs displayed a standard deviation in length of ≈22% (Figure S1, Supporting Information) and readily formed smectic-like mesophases on evaporation of their solvent. The NRs of length (670 ± 179), (533 ± 126), and (432 ± 96) nm were formed by, respectively, adding 20, 50, or 100 µL of the seed to a growth solution (see Experimental Section). The UV–vis spectra for these materials display characteristic transverse and longitudinal surface plasmon absorption modes (Figure S3, Supporting Information).[23] The position of the longitudinal SPR shifts to longer wavelengths (from 495 to 630 nm) with the decreased seed amount, resulting from the production of longer nanorods.

Temperature was found to be a key parameter in controlling the length of the Ag NRs. The Ag NR length varied nonmonotonically as a function of temperature, because although the higher temperature raises the growth rate, it also leads to more disorder, which disturbs the Ag NR growth.[24]

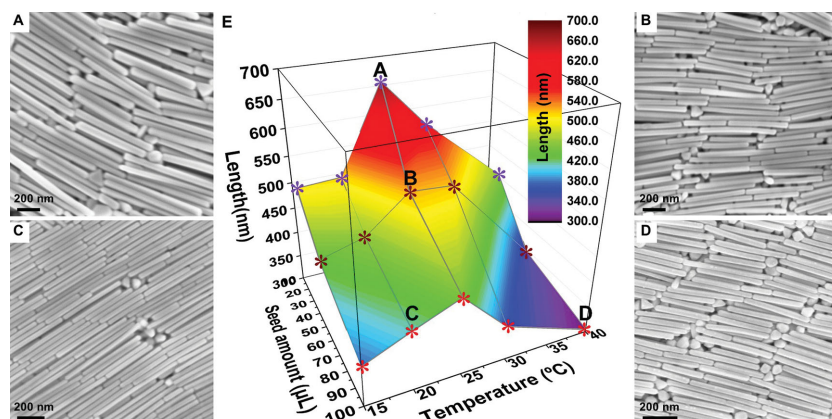Figure 1E shows the combined role of seed amount and temperature on NR length. Understanding the effect of reaction

Materials
Views
www.MaterialsViews.com

ADVANCED
FUNCTIONAL
MATERIALS
www.afm-journal.de

FULL PAPER

Figure 1. SEM images of Ag nanorods synthesized at 25 °C with different seed amounts, the number in brackets refers to the mean length and standard deviation; A) 20 µL (670 ± 179) nm; B) 50 µL (533 ± 126) nm. SEM images of Ag NRs synthesized with 100 µL seeds at different temperatures: C) 20 °C (429 ± 116) nm; D) 40 °C (305 ± 78) nm. E) The length of Ag NRs as a function of seed amount and growth temperature. All the lengths were determined by examining SEM images of the resultant Ag NRs and represent the average (and the variance) of 300 NRs. (Scale bar = 200 nm.)

parameters (i.e., seed amount and growth temperature) provides the ability to control the NR length from 300 to 700 nm with a narrow length distribution.

Gold nanotubes were formed through a room-temperature galvanic replacement reaction[25] between $AuCl_4^-$ ions and the sacrificial Ag NRs. The as-prepared Ag NRs were capped with PSS (zeta potential (−47 ± 2) mV). The PSS–Ag NRs were washed with deionized (DI) water to remove PSS molecules on the surface, then added into the aqueous solution of cetyltrimethylammonium bromide (CTAB) and sonicated for 15 min to produce positively charged CTAB–Ag NRs (zeta potential

(+55 ± 2) mV). In addition to providing a positively charged surface, the CTAB also preferentially bind to the {100} facets, which run the length of the Ag NRs, and plays a key role in the formation of the open ended NTs.[25,26]

After adding $HAuCl_4$ into the CTAB–Ag NR dispersion, the combined galvanic reaction (see reaction (1)) and Kirkendall growth lead to the formation of the Au NTs with hollow interiors and porous walls[27,28]
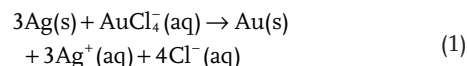
$$3Ag(s) + AuCl_4^-(aq) \rightarrow Au(s) \\ + 3Ag^+(aq) + 4Cl^-(aq) \qquad (1)$$

Figure 2A,B show the SEM and transmission electron microscopy (TEM) images of 370 nm Au NTs. The Au NTs exhibit uniform walls with pinholes. The TEM images show that the center portion of each nanostructure is lighter (i.e., less dense) than the edges, indicating the formation of hollow nanostructures (Figure 2B). The thickness of the wall is ≈6 nm, which is about one tenth of the template diameter, in good agreement with the stoichiometric relationship (i.e., three silver atoms are replaced by one Au atom, see reaction (1)). Noticeably, each NT inherits the morphological features of the Ag NRs, such as the pentagonal cross section and five straight side edges.

The selected area electron diffraction (SAED) pattern of an individual Au NT showed superpositions of ⟨110⟩ and ⟨111⟩ zones, which are consistent with a cyclic penta-twinned crystal with five {111} twin boundaries arranged radially to the [110] direction of elongation, that is, the ends of this NT are
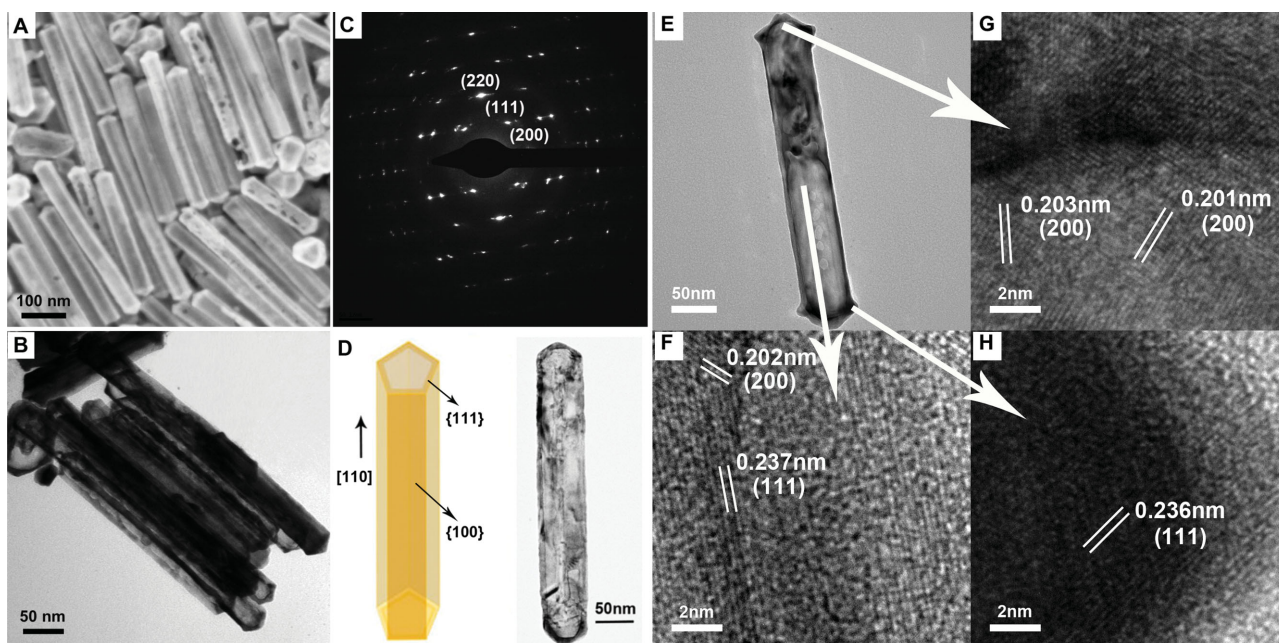

Figure 2. A) SEM and B) TEM image of Au NTs of length ≈370 nm; C) SAED pattern of an individual Au NT, D) schematic illustration of the elongated cyclic penta-tetrahedral model of Au NTs and real space (TEM) image; E) TEM image of a broken Au NT, of which the outer wall was partially detached, exposing the inner wall; F) HRTEM images of the inner wall, G) outer wall, and H) open end of the nanotube in (E).

ADVANCED
FUNCTIONAL
MATERIALS
www.afm-journal.de

Materials
Views
www.MaterialsViews.com

FULL PAPER

terminated by {111} facets, and the side surfaces are bounded by {100} facets,[29–31] providing further support for the above-mentioned morphological features observed from the real space TEM images of the Au NTs (Figure 2B,D) and the diffraction patterns from X-ray diffraction (XRD) (Figure S4, Supporting Information). Further structural information of the Au NTs (e.g., open end, cross section, inner wall, and outer wall) was obtained by sonicating the sample for 10 min to break some of the Au NTs. The resultant NTs were drop-cast onto the TEM grid. Figure 2E shows the TEM image from a typical broken gold nanotube. The outer wall of this imaged NT was partially detached, exposing the inner wall. High-resolution TEM images were taken from the middle part (Figure 2G), upper end (Figure 2F), and the lower end (Figure 2H), which correspond to the exposed inner wall, outer wall, and the open end, respectively. The fringe spacing measured from the outer wall was ≈0.20 nm, which can be assigned to the separation between (200) planes of face center-cubic gold (0.204 nm), revealing that the outer wall is dominated by the (200) planes, while the cross-section of the open end is dominated by (111) planes with the spacing ≈0.24 nm. It is noteworthy that, in addition to some regions with (200) plane, (111) planes also exist in the inner

wall. Because atoms on different crystallographic facets have different interaction strengths with a polymeric or surfactant capping reagent,[32] it can be envisaged that, when the Au NTs are utilized as drug delivery systems, the varied crystalline morphology on the inner and the outer wall will provide a possibility for differential surface modification on the two separate sides of the wall.[12]

2.2. Tunable NIR Absorbance of the Gold Nanotubes

The Au NTs exhibit absorbance peaks associated with the excitation of localized surface plasmon modes in the NIR region. The absorbance peak red-shifted with increasing nanotube length (**Figure 3**A). Boundary element method (BEM) modeling (Figure 3B) indicates that the NIR absorbance could be assigned to the superposition of the transverse mode and the first harmonic (quadrupole) longitudinal mode (labeled 1 in Figure 3B). The calculation also shows the second harmonic longitudinal mode (labeled 2) that is too weak to be resolved experimentally. Figure 3C shows that the transverse mode is insensitive to NT length while the longitudinal mode displays a distinct red shift
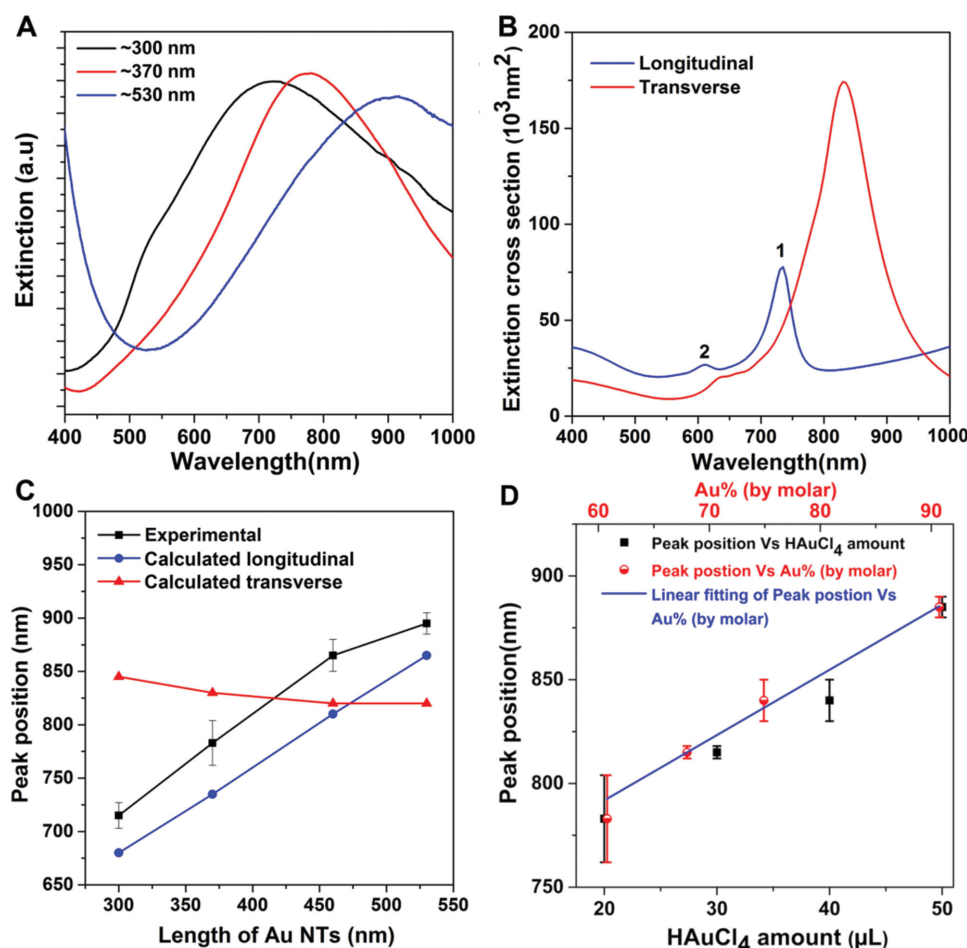

Figure 3. A) UV–vis spectra of the Au NTs of different lengths. B) BEM calculated extinction spectrum of NT of a length of ≈370 nm (outer diameter = 75 nm, wall thickness = 6 nm, Au% = 100%). The label 1 is the quadrupole longitudinal mode, and the label 2 is the octupole longitudinal mode. C) The dependence of the SPR position on the length of Au NTs (experimental and calculated). E) The dependence of the SPR position on the amount of HAuCl₄ for Au NTs (≈370 nm) and the molar composition of Au NTs.

www.MaterialsViews.com

ADVANCED
FUNCTIONAL
MATERIALS
www.afm-journal.de

FULL PAPER

with increasing nanotube length. Calculated extinction spectra for different NT lengths are shown in Figure S5, Supporting Information. While the absolute peak positions observed in the experiments are slightly different from the calculated values (possibly because of the simplified representation of the NTs selected in the modeling), both the experiment and modeling show a similar shift in the plasmon band of ≈0.78 nm (wavelength) per nm (NT length).

It was also observed that for Au NTs of a given length, the absorbance peak was red-shifted with increasing amount of $HAuCl_4$ added in the formation of Au NTs. For a NT of ≈370 nm length, the peak shifted from 775 to 880 nm by a change in $HAuCl_4$ amount from 20 to 50 µL. Similar trends have been reported for hollow Au nanospheres,[33] Au nanocages,[34] and long Au nanotubes (of micrometers in length).[35] The TEM images (Figure 2B and Figure S7, Supporting Information) in our study showed no discernable variation in the thickness with increasing amount of $HAuCl_4$, thus we ascribe the observed red-shift to the variation of elemental composition and porosity of the NTs. The elemental composition (Table S1, Supporting Information) shows a decrease in the Ag content with the increasing $HAuCl_4$ amount. Figure 3D shows a linear correlation between SPR peak position and the Au molar fraction, which is consistent with results found for Au–Ag alloy spherical nanoparticles[36] and theoretically for the Au–Ag NTs.[37] Furthermore, the reduced Ag content implies more Ag has been etched from the NTs, increasing the porosity and surface defects (as shown in Figure S7, Supporting Information), which may also contribute to the observed red-shift.[28,33,38–40]

2.3. Surface Modification of the Au NTs

The route for NT synthesis described above involved CTAB, which is highly cytotoxic and its removal from solution generally causes undesired aggregation of the nanotubes, thus hindering

potential biomedical applications.[41] Furthermore, although the CTAB–Au NTs have good stability in DI water (well-dispersed after several weeks), during a 30 min-incubation with serum-containing medium, CTAB–Au NTs agglomerate and precipitate with time, which also precludes their biological application. Therefore, surface modification is necessary to achieve biocompatible and low-cytotoxic nanotubes with colloid stability in a buffer medium. The positively charged CTAB–Au NTs were coated with negatively charged sodium polystyrenesulfonate (70 kDa) (see Experimental Section), which is commonly used as a nontoxic peptizing agent in commercial products and thus generally regarded as a safe additive.[42] After the treatment with PSS, a thin organic layer around the nanotubes was observed in TEM image (Figure S8A, Supporting Information), which is a direct visualization of polymer coating of the Au NTs.[43] The zeta potential of gold nanotubes (in DI water) changed from (45 ± 3.5) to (−43.7 ± 1.7) mV, also consistent with the successful coating of PSS on the surface of CTAB-capped Au NTs. The magnitude of the zeta potential indicates that a stable colloidal dispersion has formed. The PSS-coated NTs showed a 20 nm-red shift induced by the change in the local refractive index from that of water to that of PSS (Figure S8B, Supporting Information). PSS-coated Au NTs demonstrated excellent stability in serum-containing medium without significant absorbance loss in the NIR peak over seven days (Figure S9, Supporting Information), making them suitable for long-term culture with cells and providing the basis for further in vitro and in vivo studies.

2.4. Cytotoxicity Assessment of PSS-Coated Au NTs

Cytotoxicity of the PSS-coated gold nanotubes was assessed by using SW480 human colonic adenocarcinoma and RAW 264.7 mouse leukemic macrophage cell lines with different concentrations of nanotubes ranging from 0.068 to 50 µg mL^{-1}. As shown in **Figure 4**, SW480 cells displayed a viability of over
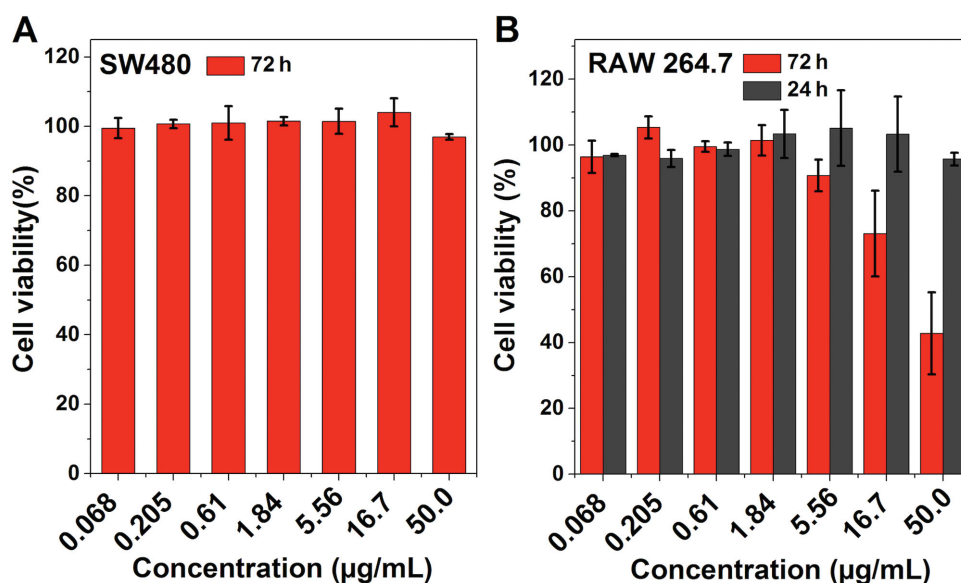

Figure 4. In vitro cell viability of SW480 cells and RAW 264.7 cells with increasing concentrations of PSS-coated Au NTs (≈370 nm in length, Au mass fraction = 73.9%). Results are shown as mean ±SD ($n = 3$) as determined using CCK-8 assays.
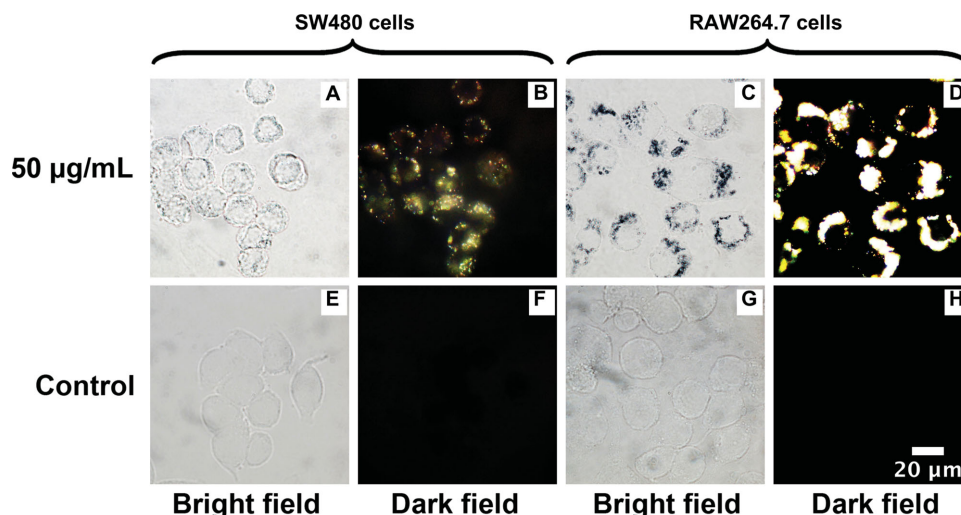
Figure 5. Bright-field and dark-field microscopy images of SW480 and RAW 264.7 cells after incubation overnight in a medium containing Au NTs (≈370 nm in length, Au mass fraction = 73.9%). All dark-field microscopy images are presented using the same brightness and contrast conditions.

90%, after 72 h incubation with Au NTs, even at high dosage (50 µg mL^{-1}). Raw 264.7 cells showed viability of ≈100% at all concentrations after 24 h exposure to NTs. The higher cytotoxicity of the Au NTs to the RAW 264.7 macrophages after 72 h at high doses (16.7 and 50 µg mL^{-1}, IC$_{50}$ = 42.35 µg mL^{-1}) compared with that to SW480 cancer cells may result from higher cellular uptake of nanoparticles into macrophages.[44]

2.5. Cellular Uptake of PSS–Au NTs

The in vitro cellular uptake of Au NTs was investigated using dark field microscopy. **Figure 5** shows the bright-field and dark-field microscopy images of SW480 and RAW 264.7 cells after incubation for 12 h in media containing Au NTs. Bright-field microscopy images (Figure 5A,C) show that cells incubated with Au NTs maintained their attachment to glass slides and their normal morphology corroborating the good biocompatibility of the PSS–Au NTs. The dark field microscopy images (Figure 5B,D) show that both SW480 and RAW 264.7 cells appear to contain Au NTs as seen by the scattered light.

Careful examination of the dark-field microscopy images shows the PSS–Au NTs enrich the cytoplasm of the cells instead of being evenly or randomly distributed on cells as it would be in the case of nonspecific adhesion, suggesting the cellular uptake of the nanotubes.[45] It was found that RAW264.7 cells possessed higher levels of NT uptake than SW480 cells, presumably because of the specialized phagocytosis of macrophage cells. These results clearly demonstrate the potential theranostic application of such PSS–Au NTs as both a bimodal (dark-field optical imaging and photoacoustic imaging which will be discussed in Section 2.7) contrast agent for bioimaging, and as vehicles for drug delivery to cancer cells or macrophage-mediated targeting. (Circulating monocytes/macrophages have a natural ability to traverse the intact and compromised blood–brain barrier and could be used as vectors to target tumors and surrounding tumor infiltrated tissue.[46,47]

2.6. In Vitro Photothermal Cell Ablation with PSS–Au NTs

Motivated by the tunable NIR absorption, low cytotoxicity, and cellular uptake of the PSS–Au NTs, their efficacy for photothermal ablation of cancer cells in vitro was investigated. Their photothermal cytotoxicity was evaluated by exposing SW480 cancer cells to a 7 ns pulsed laser with a wavelength of 800 nm at a fluence of 13 mJ cm^{-2} for 600 pulses. In the absence of PSS–Au NTs, ≈90% of SW480 cells were viable following irradiation. However, with the addition of 50 µg mL^{-1} of PSS–Au NTs, cell viability after laser illumination was reduced to (16 ± 3)% (**Figure 6**). The results shown in Figure 6 demonstrate that the PSS–Au NTs, when combined with pulsed laser excitation, cause the photothermal ablation of cancer cells in the NIR window with low doses of NTs (the highest dose used was 50 ppm). The results show that, for fixed irradiation conditions, the phototoxicity increased with increasing NTs dose. In addition, the laser fluence used was significantly below safe exposure limits for clinical use.[48]

2.7. In Vivo Photoacoustic Imaging and Biodistribution Study of PSS–Au NTs

To investigate their effectiveness as a photoacoustic image contrast agent, we performed in vivo imaging of the Au NTs using multispectral optoacoustic tomography (MSOT), which is ideally suited for detecting probes in the NIR window. A 200 µL bolus of PSS–Au NTs (25 µg Au mL^{-1}, ≈370 nm in length, Au mass fraction = 73.9%) was injected intravenously into SW620 tumor-bearing mice and images were collected at preinjection and 1 h postinjection (HPI) time points. A region of interest (ROI) consisting of transverse slices, respectively, spanning the mouse spleen–liver and tumor region was used to construct maximum intensity projection (MIP) images. **Figure 7** shows in vivo MIP images, obtained for excitation at 800 nm, at the plasmon absorbance peak of Au NTs, of the transverse slices at 1 HPI. The background-corrected images (Figure 7B,D)
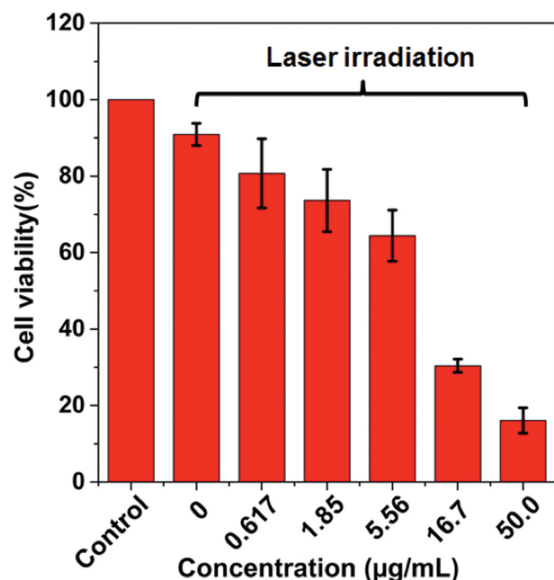
www.MaterialsViews.com

ADVANCED
FUNCTIONAL
MATERIALS
www.afm-journal.de

FULL PAPER

Figure 6. In vitro SW480 cell viability measured by CCK-8 assay ($n = 3$). SW 480 cancer cells were cultured with varied concentrations of PSS–Au NTs and then irradiated with the 7 ns pulse laser (wavelength = 800 nm) at a fluence of 13 mJ cm^{-2} per pulse for 60 s (600 pulses). Cells that were incubated in the absence of agents without irradiation were used as the control group. Results are shown as mean ±SD ($n = 3$).
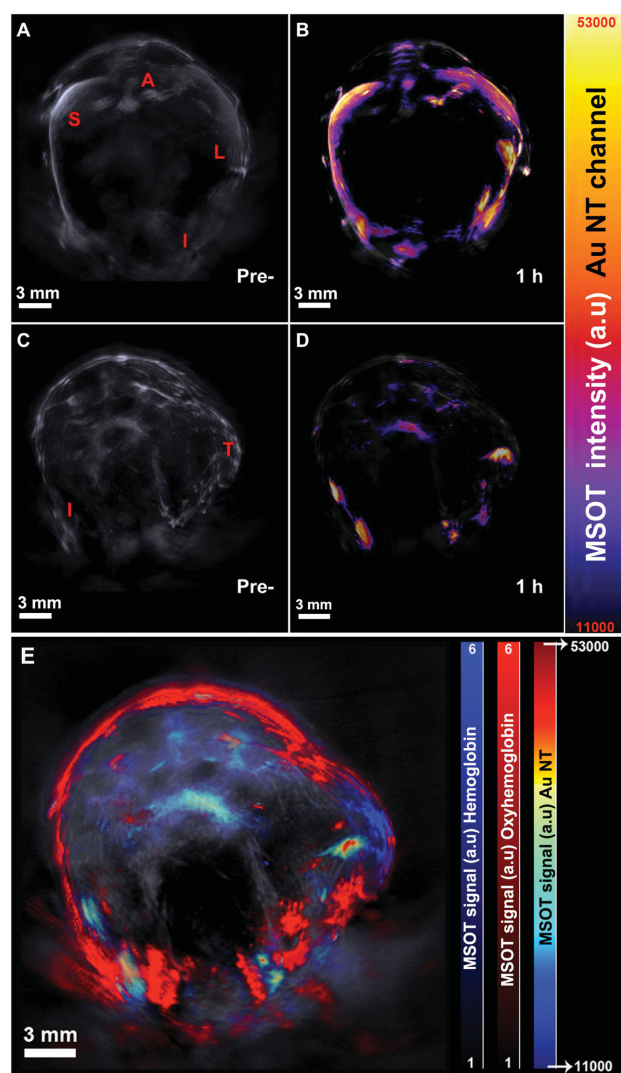

Figure 7. In vivo MSOT MIP images (single wavelength 800 nm) of transverse slices corresponding to A,B) spleen–liver region and C,D) tumor region; A,C) anatomical background (preinjection of Au NTs) image with the identification of major organs (liver (L), intestine (I), spleen (S), aorta (A), tumor (T)); B,D) background-corrected MIP image showing strong in vivo photoacoustic signal of Au NTs and the regions of high Au NT uptake at 1 h-postinjection point. E) Overlay of PSS–Au NT signal (jet scale), oxyhemoglobin signal (red scale), and hemoglobin signal (blue scale).

exhibit good contrast enhancement, which demonstrates the excellent photoacoustic signal generation capability of Au NTs through high efficiency excitation of the NIR-SPR mode. The accumulation of Au NTs in the tumor site was observed, possibly due to EPR effect (enhanced permeability and retention effect, whereby the leaky tumor vasculature contains wide interendothelial junctions and a malfunctioning lymphatic system). It was also observed that, strong in vivo MSOT signal of Au NTs was detected in the liver, spleen, and intestines. The high spatial resolution of MSOT demonstrates that the signal is localized in parts of the vessels and tissues that displayed elevated contrast on single-wavelength optoacoustic images even before the probe was injected. This suggests that probe was colocalized to contrast producing areas of accumulated blood, and considerable amount of Au NTs remained in the circulation at 1 HPI.[49] The overlay image (Figure 7E) of PSS–Au NT, oxyhemoglobin and hemoglobin signal reveal that the PSS–Au NTs are in or close to the blood vessels in the tumor, possibly due to the high interstitial fluid pressure and dense interstitial matrix,[50,51] similar to the previously reported intratumoral distribution pattern of passively targeted gold nanoparticles.[49,50] The strong MSOT signals from PSS–Au NTs observed in the tumor region at 1 HPI shows that MSOT imaging, combined with photothermal therapy, may offer a novel theranostic approach with high potential for translation to the clinics.

The whole-body longitudinal biodistribution of PSS–Au NTs was visualized and semiquantified by MSOT. A 200 µL bolus of PSS–Au NTs (25 µg Au mL^{-1}, ≈370 nm in length, Au mass fraction = 73.9%) was injected intravenously into HCT116 tumor-bearing mice and images were collected at pre- and 0.5, 24, 48, and 72 h-postinjection time points. The nonbackground-corrected orthogonal images in **Figure 8** reveal that, at 0.5 HPI,

the PSS–Au NTs showed uptake by liver and spleen, likely attributed to the macrophages residing in these tissues, and substantial increase in signal from blood that makes vessels (e.g., aorta) visible. Passive targeting and selective accumulation of nanoparticles at tumor sites depend on the degree of tumor vascularization and porosity.[52] In this biodistribution study with HCT116 tumor lacking extensive vascularization,[53,54] no accumulation of PSS–Au NTs at the tumor site was observed. (Figure S11, Supporting Information, resolves the contributions from oxygenated and deoxygenated hemoglobin within the tumor,[49,50] and shows limited oxyhemoglobin signal in the HCT116 tumor, indicating a lack of vasculature required for probe delivery and providing a possible explanation for the
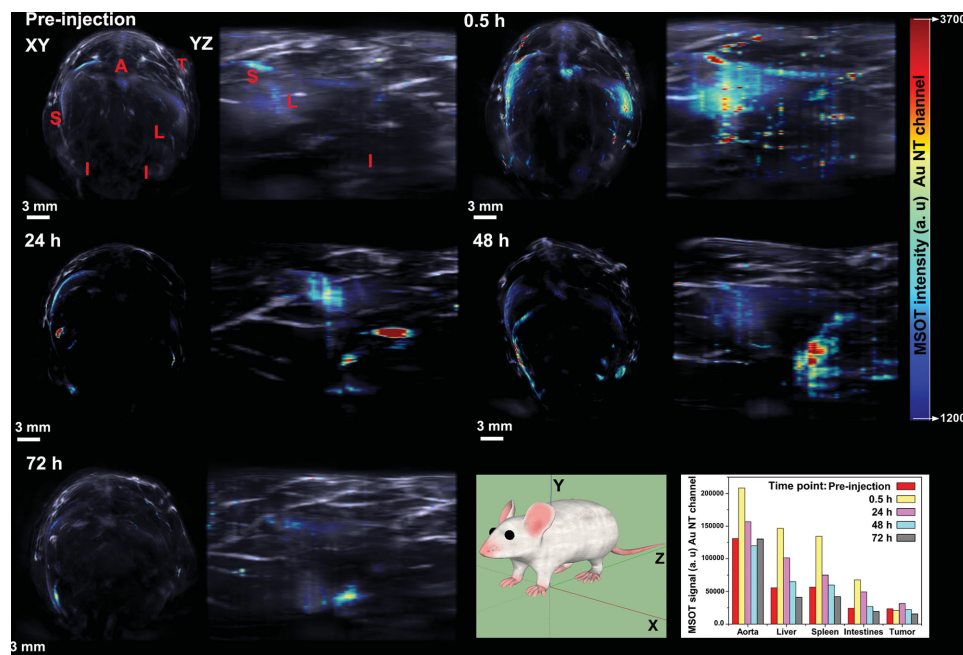
ADVANCED
FUNCTIONAL
MATERIALS
www.afm-journal.de

Materials
Views
www.MaterialsViews.com

Figure 8. In vivo nonbackground-corrected orthogonal images of HCT 116 tumor-bearing mice at varied time points after tail-vein injection of PSS–Au NTs. (The cartoon in the inset shows the 3D coordinate system defining the orientations of the orthogonal views), (liver (L), intestine (I), spleen (S), aorta (A), tumor (T)) and quantifications of the MSOT signal intensity in aorta, different organs, and tumor at different time points postinjection.

absence of the probe inside the tumor.[49] The MSOT signal of Au NTs transferred from liver and spleen to intestine at 24 and 48 HPI and then decreased to the preinjection level at 72 HPI, suggesting probe clearance via the hepatobiliary system within 72 h.

2.8. Ex Vivo Analysis of the Mice Injected with PSS–Au NTs

Histological analysis of the major organs (liver, spleen) was performed on tissues harvested at 72 h postinjection of the Au NTs. No apparent tissue/cellular damages were observed in the mice injected with Au NTs. No overt pathological changes were observed in the spleen or liver. As seen in Figures S12 and S13, Supporting Information, in the dark-field microscopy images of these tissues, the light scattering signal of Au or Ag was absent, confirming the clearance of the Au NTs from these organs at 72 HPI, in agreement with in vivo MSOT imaging results. We postulate that the abundant surface charge of the PSS–Au NTs make them amenable to hepatobiliary excretion into the gastrointestinal tract.[55] It is known that most nanoparticles tend to exhibit high uptake in the reticuloendothelial system of liver and spleen upon intravenous administration and are not rapidly degraded or excreted. To best minimize toxicity and/or collateral effects, a nanoparticle should either be degraded in situ into truly noncytotoxic subcomponents or be excreted from the body, once it has served its diagnostic/therapeutic purpose.[56] Therefore, the strong in vivo MSOT signals from the Au NTs and the rapid hepatobiliary excretion will endow applicability as efficient and safe probes for in vivo bioimaging.

3. Conclusion

We have developed a route for the length-controlled synthesis of hollow gold nanotubes with well-defined shape, high crystallinity, and strong surface plasmon absorbance bands in NIR region. The length control was achieved by adjusting both the seed amount and growth temperature in the synthesis of Ag NR templates. The resultant Au NTs had ≈6 nm thick walls and open ends. The inner and outer walls had distinct crystalline structures, which will facilitate differential surface functionalization for the future. By varying the gold salt amount during NT growth, we have further shown that the Au content in the nanotubes could be controlled in a systematic way providing an alternative means for tuning the optical and plasmonic properties.

The Au NTs have been engineered by PSS coating, leading to the formation of a nanosystem with good colloidal stability in cell culture medium, low cytotoxicity, cellular uptake by cancer cells and macrophage cells, and photothermal ablation of cancerous cells, offering the potential to be further developed for in vivo bioimaging or theranostic application.

MSOT was used to evaluate the in vivo capability to visualize the PSS–Au NTs and their biodistribution. The intravenously injected PSS–Au NTs have shown excellent photoacoustic signal enhancement and the accumulation at the SW620 tumor site. The biodistribution study shows that the PSS–Au NTs undergo hepatobiliary clearance over a period of 72 h.

Taken together, these results demonstrate that Au NTs can be applied as a safe and effective theranostic system for photothermal therapy and photoacoustic imaging, as well as a promising drug delivery vehicle. In future studies, more work will

www.MaterialsViews.com

ADVANCED
FUNCTIONAL
MATERIALS
www.afm-journal.de

FULL PAPER

be devoted toward active targeting of the Au NTs to tumor site. One can envision the further development of gold nanotube-based nanosystems which enable simultaneous visualization and delivery of therapeutic agents combined with high-resolution imaging modalities and photothermal therapy function, holding great potential for further clinical application.
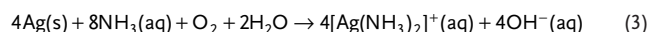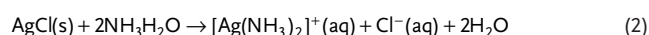
4. Experimental Section

Materials: Gold (III) chloride trihydrate (520918), CTAB (H6269), ammonium hydroxide solution (NH_3 in H_2O), Cell Count Kit-8 (CCK-8, 96992-500TESTS-F) were purchased from Sigma-Aldrich. Silver nitrate (11414), trisodium citrate, anhydrous (45556), L-(+)-ascorbic acid (A15613) were purchased from Alfa Aesar. PSS, MW 70 000 (10328550), sodium borohydride ($NaBH_4$, 10599010), hydrochloric acid (37%, UN1789), and nitric acid (70%, UN2031) were purchased from Fisher Scientific. All chemicals were used without further purification.

Characterizations: The UV–vis absorption spectra were recorded with a Perkin–Elmer Model Lambda35 spectrophotometer. SEM images were obtained using a LEO 1530 Gemini FEGSEM. Each SEM sample was prepared by placing 5 μL nanoparticle dispersion (in Milli-Q) onto an aluminium substrate and drying under room temperature naturally. A TEM (Tecnai G^2 Spirit TWIN/BioTWIN) with an acceleration voltage of 120 kV was used to take lower resolution TEM images. A field emission gun TEM microscope (Philips CM200 FEGTEM; 200 kV) equipped with a Gatan GIF200 imaging filter running DigitalMicrograph software was used to take higher magnification TEM images and energy dispersive X-ray spectroscopy (EDX). For preparing for the TEM samples, 5 μL nanoparticle dispersion (in Milli-Q) was dropped onto a carbon-coated copper grid and dried at room temperature naturally. A Malvern Zetasizer-Nano Series-Zen 3600 was used to perform zeta potential measurements. A minimum of 20 measurements was acquired for each sample. The XRD pattern was obtained by using a Panalytical Model X'Pert Pro MPD X-ray diffractometer with Cu Kα source and an X'cellerator detector. A continuous scan over a 2θ range from 30° to 90° was performed with an acquisition time of 1 h per sample at a step size of 0.05°, samples were prepared by depositing and drying slurries directly on low-background Si sample holders. The concentration of Au nanotubes (Au and Ag content) in solution was determined using an atomic absorption spectrometer (AAS, Varian 240fs).

Reaction Preparation: Vials and stir bars were cleaned with aqua regia (nitric acid and hydrochloric acid in a volume ratio of 1:3) thoroughly rinsed with DI water, and dried in an 80 °C oven before use. Once dry, the flasks were allowed to cool to room temperature before any reactants were added.

Synthesis of Ag NRs: 1) Preparation of Ag seed: The freshly prepared $AgNO_3$ aqueous solution (250 μL, 10×10^{-3} M) and trisodium citrate aqueous solution (500 μL, 5×10^{-3} M) were added sequentially into 9.250 mL Milli-Q to form a 10 mL solution with a final concentration of 0.25×10^{-3} M $AgNO_3$ and 0.25×10^{-3} M trisodium citrate, into which an aqueous solution of $NaBH_4$ (0.3 mL, 10×10^{-3} M, freshly prepared and kept in 4 °C refrigerator for 3 h before use) was injected with vigorous magnetic stirring. Stirring was stopped after 30 s. The as-formed seed was incubated at 21 °C in dark for 2 h. (In our experiments, few Ag nanorods were formed when the seed was incubated at temperature higher than 25 °C.) 2) Growth of Ag nanorods: the freshly prepared $AgNO_3$ aqueous solution (200 μL, 8×10^{-3} M) and ascorbic acid aqueous solution (400 μL, 100×10^{-3} M), Ag seeds (20, 50, or 100 μL) were added sequentially into 21.7×10^{-3} M PSS aqueous solution (7.44 mL, 21.7×10^{-3} M, the concentration of PSS was calculated according to its monomer unit. The solution was kept at corresponding growth temperature for 30 min) without stirring. After an undisturbed growth for 10 min at a certain temperature (15, 20, 25, 30, or 40 °C), the reaction products were isolated by centrifugation at 4000 rpm (3005 g) for 10 min followed by removal of the supernatant. The Ag NR pellet was redispersed in Milli-Q.

Formation of Au NTs: The as-synthesized Ag NRs were washed with Milli-Q for three times via centrifugation (at 4000 rpm for 8 min for each time). The final Ag NR pellet was mixed with 330 μL of CTAB aqueous solution (20×10^{-3} M), and then sonicated for 15 min. 0.02 M $HAuCl_4$ aqueous solution (20, 30, 40, or 50 μL) was slowly added dropwise to the CTAB–Ag NR solution. The reaction was allowed to proceed at room temperature for 30 min and magnetic stirring was used throughout the synthesis. The resultant solution was centrifuged at 5000 rpm (4696 g) for 8 min and the supernatant was removed. The pellet was washed with CTAB aqueous solution (10×10^{-3} M) and $NH_3 \cdot H_2O$ (33%) subsequently, then redispersed in 200 μL $NH_3 \cdot H_2O$ and kept for overnight to further remove the AgCl,[57] according to reaction (2) (some Ag was also removed by treatment with $NH_3 \cdot H_2O$, following reaction (3)[58]). The mixture was centrifuged (5000 rpm, 8 min) and washed with CTAB aqueous solution (0.01 M) twice. The final product of Au NTs was collected in Milli-Q. The synthesis was scaled up by tenfold to yield the gold nanotubes for in vitro and in vivo studies

$$AgCl(s) + 2NH_3H_2O \rightarrow [Ag(NH_3)_2]^+(aq) + Cl^-(aq) + 2H_2O \qquad (2)$$

$$4Ag(s) + 8NH_3(aq) + O_2 + 2H_2O \rightarrow 4[Ag(NH_3)_2]^+(aq) + 4OH^-(aq) \qquad (3)$$

Surface Modification with PSS: A CTAB–Au NTs suspension (O.D. ≈1) was added dropwise into the solution of PSS solution (10 mg mL^{-1}) and NaCl (5×10^{-3} M) in a 1:1 volume ratio and allowed to react for one day (magnetic stirring was used throughout the reaction). The nanotubes were then collected by centrifugation (5000 rpm, 15 min), the supernatant was decanted, and the Au NTs were redispersed in an aqueous solution of unadulterated PSS (1 mg mL^{-1}, the same volume as the original suspension of CTAB–Au NTs). The centrifugation (5000 rpm, 15 min)–redispersion cycle was repeated twice to yield PSS-coated Au NTs suspensions with minimal cytotoxicity. The resultant PSS–Au NTs suspension (in unadulterated PSS solution) was centrifuged (5000 rpm, 15 min) and redispersed in Milli-Q for future use.

Cell Culture: SW480 cells (SW480 ATCC CCL-228, Invitrogen Life Technologies) and RAW 264.7 cells (ATCC-TIB-71, Invitrogen Life Technologies) were cultured in RPMI 1640 medium (61870-010, Life Technologies) with 10% fetal bovine serum at 37 °C in a humidified atmosphere of 5% CO_2 in air.

Cytotoxicity Assay: The CCK-8 cell viability assays were performed according to the manufacturer's instructions. Cells were seeded in 96-well plates (3599, Corning) at a density of 5000 cells/well. After incubation for 24 h at 37 °C in 100 μL culture medium (RPMI 1640), 10 μL of culture medium containing varied concentrations of PSS–Au NTs was added into each well (the concentration in Section 2 represents the final concentration of PSS Au NTs in the well). After incubation for 72 h (or 24 h), 10 μL CCK-8 solution was added in each well, followed by incubation for another 4 h. The absorbance was monitored at 450 nm on a microplate reader (Mithras LB 940). The cytotoxicity was expressed as the percentage of the cell viability as compared with the blank control. A culture medium (without cells) containing PSS–Au NTs at corresponding concentration was used as the background, the optical density of which was subtracted for eliminating the absorption interference of samples. For each condition, the experiment was performed in triplicate with the result of each individual experiment derived from six wells.

Dark-Field Microscopy Imaging: Cells were plated onto 20 mm glass coverslips in a six-well plate (Corning, 3516) at a certain density (2×10^5 for SW 480 cells and 1×10^5 for Raw 264.7 cells) and allowed to grow for two days. Then the medium was replaced with 2 mL of a medium containing PSS–Au NTs at different concentrations. After incubation for 12 h, the medium was removed and the cell monolayer on the coverslip was rinsed with DPBS twice (14190-094, Life Technologies), fixed in 4% paraformaldehyde/DPBS for 10 min at room temperature, and rinsed with DPBS twice. The fixed coverslips were mounted and sealed onto glass slides. Bright and dark field microscopy imaging was performed with an inverted microscope (Nikon Eclipse Ti-E, Nikon UK Limited,

Surrey, UK) and an oil coupled 100′ objective (CFI Plan Fluor, Nikon UK Limited, Surrey, UK). Images were recorded using a 5 Megapixel color camera (DS-Fi1, Nikon UK Limited, Surrey, UK) and saved using the NIS-Elements D software.

In Vitro Photothermal Cell Ablation with PSS–Au NTs: SW480 cells were seeded onto 96-well plates (5000 cells/well) and incubated in 100 µL of medium (per well) at 37 °C in a humidified atmosphere with 5% CO_2 for 24 h. Then the cells were treated with different concentrations of PSS–Au NTs. After 4 h incubation, the cells were exposed to a 7 ns pulsed OPO (optical parametric oscillator) laser (Surelite OPO Plus, Continuum, Santa Clara, CA, USA). The output of the 7 ns pulsed OPO laser was tuned to a wavelength of 800 nm, attenuated then coupled into a fiber optic cable (BF20LSMA02, ThorLabs Inc., Newton, NJ, USA). The fiber output was positioned to illuminate the bottom of a single well of a 96-well plate, where the beam width was 7 mm and a fluence of 13 mJ cm^{-2}. The plates were mounted on a three-axis computer controlled gantry system (Zolix Instruments Co., Beijing, China), where each well was exposed to the laser for 60 s, i.e., 600 laser pulses (10 Hz pulse repetition frequency). Following the laser exposure, the cells were further incubated for 24 h and then 10 µL of the CCK-8 solution was added to each well of the plate, followed by incubation for another 3 h. Then, cell viability was determined by measuring absorbance at the wavelength of 450 nm with a microplate reader. The experiment was performed in triplicate with the result of each individual experiment derived from six wells.

In Vivo Photoacoustic Imaging and Biodistribution Study: The colorectal cell line, SW620 was grown in Roswell Park Memorial Institute medium 1640 (RPMI Medium 1640, GIBCO) supplemented with 10% (v/v) fetal calf serum in 5% CO_2 at 37 °C. 1×10^7 cells were collected in 100 µL of phosphate buffered saline and injected subcutaneously into the right flack of 12-week-old female CD1 nude mice to form xenografts. The colorectal cancer cell line, HCT116 was grown in Dulbecco's modified eagle medium (DMEM, Invitrogen) supplemented with 10% (v/v) fetal calf serum, and 4 µL mL^{-1} Hygromycin B (Sigma, Poole U.K.) in 5% CO_2 at 37 °C. 1×10^6 cells were collected in 100 µL of serum-free DMEM and injected subcutaneously into the right flank of 8–10-week-old female CD1 nude mice to form xenografts. All experiments were performed following local ethical approval and in accordance with the Home Office Animal Scientific Procedures Act 1986. A real-time MSOT scanner was utilized in this study (MSOT inVision 128, iThera Medical Germany). The animal was anesthetized with isofluorane and placed in supine position inside the imaging chamber. 200 µL of PSS–Au NTs (25 µg mL^{-1}) was injected via a catheter into the tail vein of tumor-bearing anesthetized mice and the probe biodistribution was monitored over time in various organs using PA imaging. Before image acquisition, a volume ROI consisting of transverse slices with a step size of 0.5 mm spanning from the liver to the lower abdomen was selected by manual inspection of live MSOT images, and the laser excitation wavelengths of 715, 730, 760, 800, 830, 850, and 900 nm were selected corresponding to the major turning points in the absorption spectra of PSS–Au NTs, oxy-hemoglobin and hemoglobin. Multispectral imaging was then performed with ten signal averages per wavelength per transverse slice at different time points. Images were reconstructed using a model-based approach for offline analysis. After image reconstruction, spectral unmixing was performed to resolve individual components from different chromophores in the system. For each pixel in the image, the method fits the total measured optoacoustic spectrum to the known absorption spectra of the individual chromophores, based on linear regression. Maximum intensity projection (MIP) images were presented. For the later time points (24, 48, and 72 h), the background subtraction is not possible, as the animal is removed and placed in the MSOT system repeatedly, with repositioning, in order to avoid over dosage of isoflurane for the entire duration.

Ex Vivo Analysis: The major organs such as liver and spleen were harvested and fixed in 4% (w/v) paraformaldehyde in PBS overnight. After processing and embedding in wax, sections were dewaxed, rehydrated, and stained with haematoxylin and eosin. The histological sections were observed with an optical microscope with different combinations of magnifications and objective lens.

Supporting Information

Supporting Information is available from the Wiley Online Library or from the author.

Acknowledgements

[1] S. K. Maji, S. Sreejith, J. Joseph, M. Lin, T. He, Y. Tong, H. Sun, S. W.-K. Yu, Y. Zhao, *Adv. Mater.* **2014**, *26*, 5633.

[2] V. Ntziachristos, D. Razansky, *Chem. Rev.* **2010**, *110*, 2783.

[3] H. Gong, L. Cheng, J. Xiang, H. Xu, L. Feng, X. Shi, Z. Liu, *Adv. Funct. Mater.* **2013**, *23*, 6059.

[4] J. Chen, M. Yang, Q. Zhang, E. C. Cho, C. M. Cobley, C. Kim, C. Glaus, L. V. Wang, M. J. Welch, Y. Xia, *Adv. Funct. Mater.* **2010**, *20*, 3684.

[5] E. C. Dreaden, A. M. Alkilany, X. Huang, C. J. Murphy, M. A. El-Sayed, *Chem. Soc. Rev.* **2012**, *41*, 2740.

[6] K. H. Song, C. Kim, C. M. Cobley, Y. Xia, L. V. Wang, *Nano Lett.* **2009**, *9*, 183.

[7] X. Huang, S. Neretina, M. A. El-Sayed, *Adv. Mater.* **2009**, *21*, 4880.

[8] R. Bardhan, S. Lal, A. Joshi, N. J. Halas, *Acc. Chem. Res.* **2011**, *44*, 936.

[9] M. P. Melancon, M. Zhou, C. Li, *Acc. Chem. Res.* **2011**, *44*, 947.

[10] Y. Xia, W. Li, C. M. Cobley, J. Chen, X. Xia, Q. Zhang, M. Yang, E. C. Cho, P. K. Brown, *Acc. Chem. Res.* **2011**, *44*, 914.

[11] C. R. Martin, P. Kohli, *Nat. Rev. Drug Discovery* **2003**, *2*, 29.

[12] A. Nan, X. Bai, S. J. Son, S. B. Lee, H. Ghandehari, *Nano Lett.* **2008**, *8*, 2150.

[13] J.-W. Kim, E. I. Galanzha, E. V. Shashkov, H.-M. Moon, V. P. Zharov, *Nat. Nanotechnol.* **2009**, *4*, 688.

[14] X. Huang, X. Peng, Y. Wang, Y. Wang, D. M. Shin, M. A. El-Sayed, S. Nie, *ACS Nano* **2011**, *5*, 6765.

[15] P. Kolhar, A. C. Anselmo, V. Gupta, K. Pant, B. Prabhakarpandian, E. Ruoslahti, S. Mitragotri, *Proc. Natl. Acad. Sci. U.S.A.* **2013**, *110*, 10753.

[16] E. C. Dreaden, M. A. Mackey, X. Huang, B. Kang, M. A. El-Sayed, *Chem. Soc. Rev.* **2011**, *40*, 3391.

[17] S. K. Balasubramanian, J. Jittiwat, J. Manikandan, C.-N. Ong, L. E. Yu, W.-Y. Ong, *Biomaterials* **2010**, *31*, 2034.

[18] L. Guo, I. Panderi, D. D. Yan, K. Szulak, Y. Li, Y.-T. Chen, H. Ma, D. B. Niesen, N. Seeram, A. Ahmed, B. Yan, D. Pantazatos, W. Lu, *ACS Nano* **2013**, *7*, 8780.

[19] Y. G. Sun, B. T. Mayers, Y. N. Xia, *Nano Lett.* **2002**, *2*, 481.

[20] H. Jang, Y.-K. Kim, H. Huh, D.-H. Min, *ACS Nano* **2014**, *8*, 467.

[21] S. H. Han, J.-S. Lee, *Langmuir* **2012**, *28*, 828.

www.MaterialsViews.com

ADVANCED
FUNCTIONAL
MATERIALS
www.afm-journal.de

FULL PAPER

[22] N. R. Jana, L. Gearheart, C. J. Murphy, *Chem. Commun.* **2001**, 617.

[23] M. A. Mahmoud, M. A. El-Sayed, J. Gao, U. Landman, *Nano Lett.* **2013**, *13*, 4739.

[24] R. Becker, B. Liedberg, P.-O. Kall, *J. Colloid Interface Sci.* **2010**, *343*, 25.

[25] Y. Bi, G. Lu, *Nanotechnology* **2008**, *19*, 275306.

[26] D. Fava, Z. Nie, M. A. Winnik, E. Kumacheva, *Adv. Mater.* **2008**, *20*, 4318.

[27] E. Gonzalez, J. Arbiol, V. F. Puntes, *Science* **2011**, *334*, 1377.

[28] A. M. Goodman, Y. Cao, C. Urban, O. Neumann, C. Ayala-Orozco, M. W. Knight, A. Joshi, P. Nordlander, N. J. Halas, *ACS Nano* **2014**, *8*, 3222.

[29] C. J. Johnson, E. Dujardin, S. A. Davis, C. J. Murphy, S. Mann, *J. Mater. Chem.* **2002**, *12*, 1765.

[30] E. Carbo-Argibay, B. Rodriguez-Gonzalez, I. Pastoriza-Santos, J. Perez-Juste, L. M. Liz-Marzan, *Nanoscale* **2010**, *2*, 2377.

[31] H. Y. Chen, Y. Gao, H. R. Zhang, L. B. Liu, H. C. Yu, H. F. Tian, S. S. Xie, J. Q. Li, *J. Phys. Chem. B* **2004**, *108*, 12038.

[32] Y. G. Sun, B. Mayers, T. Herricks, Y. N. Xia, *Nano Lett.* **2003**, *3*, 955.

[33] H.-N. Xie, I. A. Larmour, Y.-C. Chen, A. W. Wark, V. Tileli, D. W. McComb, K. Faulds, D. Graham, *Nanoscale* **2013**, *5*, 765.

[34] S. E. Skrabalak, L. Au, X. Li, Y. Xia, *Nat. Protoc.* **2007**, *2*, 2182.

[35] Y. G. Sun, Y. N. Xia, *J. Am. Chem. Soc.* **2004**, *126*, 3892.

[36] S. Link, Z. L. Wang, M. A. El-Sayed, *J. Phys. Chem. B* **1999**, *103*, 3529.

[37] J. Zhu, *J. Phys. Chem. C* **2009**, *113*, 3164.

[38] Y. G. Sun, Y. N. Xia, *Nano Lett.* **2003**, *3*, 1569.

[39] Y. G. Sun, Y. Wang, *Nano Lett.* **2011**, *11*, 4386.

[40] N. R. Sieb, N.-C. Wu, E. Majidi, R. Kukreja, N. R. Branda, B. D. Gates, *ACS Nano* **2009**, *3*, 1365.

[41] L. Vigderman, P. Manna, E. R. Zubarev, *Angew. Chem. Int. Ed.* **2012**, *51*, 636.

[42] A. P. Leonov, J. Zheng, J. D. Clogston, S. T. Stern, A. K. Patri, A. Wei, *ACS Nano* **2008**, *2*, 2481.

[43] A. Gole, C. J. Murphy, *Chem. Mater.* **2005**, *17*, 1325.

[44] R. Weissleder, M. Nahrendorf, M. J. Pittet, *Nat. Mater.* **2014**, *13*, 125.

[45] R. Guo, L. Zhang, H. Qian, R. Li, X. Jiang, B. Liu, *Langmuir* **2010**, *26*, 5428.

[46] E. C. Dreaden, S. C. Mwakwari, L. A. Austin, M. J. Kieffer, A. K. Oyelere, M. A. El-Sayed, *Small* **2012**, *8*, 2819.

[47] S.-K. Baek, A. R. Makkouk, T. Krasieva, C.-H. Sun, S. J. Madsen, H. Hirschberg, *J. Neurooncol.* **2011**, *104*, 439.

[48] ANSI, Z136.1 Safe Use of Lasers, **2007**.

[49] E. Herzog, A. Taruttis, N. Beziere, A. A. Lutich, D. Razansky, V. Ntziachristos, *Radiology* **2012**, *263*, 461.

[50] W. Wu, W. Driessen, X. Jiang, *J. Am. Chem. Soc.* **2014**, *136*, 3145.

[51] E. A. Sykes, J. Chen, G. Zheng, W. C. W. Chan, *ACS Nano* **2014**, *8*, 5696.

[52] M. K. Yu, J. Park, S. Jon, *Theranostics* **2012**, *2*, 3.

[53] N. Y. Rapoport, Z. Gao, P. Kamaev, D. A. Christensen, *Therapeutic Ultrasound*, Vol. *829*, (Eds: G. T. Clement, N. J. McDannold, K. Hynynen), American Institute of Physics, New York, USA **2006**, p 481.

[54] J. S. Burre, S. Walker-Samuel, L. C. J. Baker, J. K. R. Boult, A. J. Ryan, J. C. Waterton, J. Haiday, S. P. Robinson, *Magn. Reson. Med.* **2011**, *66*, 227.

[55] J. S. Souris, C.-H. Lee, S.-H. Cheng, C.-T. Chen, C.-S. Yang, J.-A. A. Ho, C.-Y. Mou, L.-W. Lo, *Biomaterials* **2010**, *31*, 5564.

[56] R. Kumar, I. Roy, T. Y. Ohulchanskyy, L. A. Vathy, E. J. Bergey, M. Sajjad, P. N. Prasad, *ACS Nano* **2010**, *4*, 699.

[57] Y. Sun, *Nanoscale* **2010**, *2*, 1626.

[58] S. E. Hunyadi, C. J. Murphy, *J. Mater. Chem.* **2006**, *16*, 3929.